

# Dust sub-mm emission in Green Valley galaxies

Massimiliano Parente<sup>1,2,3</sup>, Cinthia Ragone-Figueroa<sup>4,2,3</sup>, Gian Luigi Granato<sup>2,3,4</sup>, Laura Silva<sup>2,3</sup>,  
Valeria Coenda<sup>4,5</sup>, Héctor J. Martínez<sup>4,5</sup>, Hernán Muriel<sup>4,5</sup>, and Andrea Lapi<sup>1,3,6,7</sup>

<sup>1</sup> SISSA, Via Bonomea 265, I-34136 Trieste, Italy

<sup>2</sup> INAF, Osservatorio Astronomico di Trieste, via Tiepolo 11, I-34131, Trieste, Italy

<sup>3</sup> IFPU, Institute for Fundamental Physics of the Universe, Via Beirut 2, 34014 Trieste, Italy

<sup>4</sup> IATE - Instituto de Astronomía Teórica y Experimental, Consejo Nacional de Investigaciones Científicas y Técnicas de la República Argentina (CONICET), Universidad Nacional de Córdoba, Laprida 854, X5000BGR, Córdoba, Argentina

<sup>5</sup> Observatorio Astronómico, Universidad Nacional de Córdoba, Laprida 854, X5000BGR, Córdoba, Argentina

<sup>6</sup> INFN, Istituto Nazionale di Fisica Nucleare, Via Valerio 2, I-34127, Trieste, Italy

<sup>7</sup> INAF/IRA, Istituto di Radioastronomia, Via Piero Gobetti 101, 40129 Bologna, Italy

e-mail: mparente@sissa.it - massimiliano.parente@inaf.it

Received XXX; Accepted YYY

## ABSTRACT

**Context.** Green valley (GV) galaxies are objects defined on a color–magnitude, or color–mass, diagram which are associated with a transition from a star-forming to a quiescent state (quenching), or vice versa (rejuvenation).

**Aims.** We study the sub-mm emission of galaxies in the GV and link it with their physical evolutionary properties.

**Methods.** We exploit a semi-analytic model (SAM) for galaxy evolution which includes a detailed treatment of dust production and evolution in galactic contexts. We model the observational properties of simulated galaxies by post-processing the SAM catalogs with the spectral synthesis and radiative transfer code GRASIL.

**Results.** Our model produces a clear bimodality (and thus a GV) in the color–mass diagram, although some tensions arise when compared to observations. After having introduced a new criterion for identifying the GV in any dataset, we find that most blue and GV galaxies in our model are emitters at  $250\ \mu\text{m}$  (with fluxes  $\geq 25\ \text{mJy}$ ), in keeping with GAMA results. In the color- $S_{250\ \mu\text{m}}$  diagram, GV galaxies exhibit intermediate colors yet maintain significant sub-mm fluxes. This occurs because, while specific star formation rates drop sharply during quenching, the dust content remains relatively high during the GV transition, powering sub-mm emission. Rejuvenating galaxies in the GV, which were previously red, have experienced a star formation burst that shifts their color to green, but their  $S_{250\ \mu\text{m}}$  fluxes remain low due to still low dust mass.

**Conclusions.** Our galaxy evolution model highlights the delay between star formation and dust evolution, showing that sub-mm emission is not always a safe indicator of star formation activity, with quenching (rejuvenating) GV galaxies featuring relatively large (low) sub-mm emission.

**Key words.** Galaxies: evolution – ISM: dust, extinction – Submillimeter: galaxies

## 1. Introduction

The "Green Valley" (GV; Wyder et al. 2007) in galaxy evolution refers to the transitional region on a color–magnitude (or color–mass) diagram that lies between the blue cloud (BC) of star-forming galaxies and the red sequence (RS) of passive galaxies. This valley is believed to result from the relatively rapid transition of galaxies from the star-forming state to a passive one, making it crucial for understanding galaxy quenching processes (see Salim 2014 for a review). However, some inactive galaxies can experience "rejuvenation", a phase where they undergo a new burst of star formation after a period of minimal activity. This rejuvenation can move galaxies in the red sequence back into the GV, and in some cases, even into the blue cloud (e.g., Graham et al. 2017; Rowlands et al. 2018; Chauke et al. 2019).

Defining the GV is a complex task. Traditional approaches often rely on color to define the GV (e.g., Brammer et al. 2009; Schawinski et al. 2014; Gu et al. 2018), but this can lead to systematic errors due to dust attenuation. Salim (2014) highlights the use of the UV-optical color–magnitude diagram to identify the GV, which effectively distinguishes between star-forming

and quiescent galaxies without the biases of optical colors. An alternative method proposed by Anghopo et al. (2019) employs the  $4000\ \text{\AA}$  break strength, offering a dust-insensitive metric. Nyiransengiyumva et al. (2021), emphasize that different GV selection criteria can lead to variations in the resulting galaxy populations in terms of color, specific star formation rate (sSFR), or star formation rate (SFR), demonstrating the challenges in defining the GV. More recently, Pandey (2024) introduced a novel definition using entropic thresholding on the color–stellar mass plane, which provides a natural boundary for the GV. This wide array of methods and data, ranging from spectroscopic analyses of the Sloan Digital Sky Survey (SDSS) to UV observations from GALEX, underscores both the complexity and importance of accurately defining the GV for studies of galaxy evolution.

Despite the various methods used to identify GV galaxies, they all share the common goal of identifying galaxies transitioning from a star-forming state to a quiescent, passive state. The properties of these GV galaxies can provide insights into the mechanisms driving quenching, such as halo heating (Marasco et al. 2012), supernova-driven winds (e.g., Bower et al. 2012;

Stringer et al. 2012), feedback from massive stars (e.g., Dalla Vecchia & Schaye 2008; Hopkins et al. 2012), and Active Galactic Nuclei (AGN) feedback (e.g., Granato et al. 2004; Di Matteo et al. 2005; Nandra et al. 2007; Hasinger 2008; Silverman et al. 2008; Cimatti et al. 2013). AGN feedback, in particular, has often been pointed out to play a relevant role due to the higher prevalence of AGNs in GV galaxies compared to those in the blue or red sequences (Gu et al. (2018); Schawinski et al. (2010); Wang et al. (2017); Lacerda et al. (2020); but see also Mahoro et al. 2022). Additionally, external quenching mechanisms, such as ram pressure and strangulation, can also drive the transition in the color–magnitude diagram, making the environment in which galaxies reside another crucial factor in shaping the GV transition (e.g. Lin et al. 2019; Bluck et al. 2020; Trussler et al. 2020; Sampaio et al. 2022). Numerous studies have shown that denser environments and galaxy groups facilitate more efficient quenching (Coenda et al. 2018; González Delgado et al. 2022; Chang et al. 2022).

Numerical simulations have been widely used to study the transition of galaxies within the GV. The insights from these theoretical models, such as NIHAO, Illustris TNG, and EAGLE, indicate that AGN feedback is the primary mechanism driving the GV transition (e.g., Blank et al. 2022; Anghoip et al. 2021). These simulations also offer valuable information on the timescales required for this transition, often referred to as quenching timescales, and how these relate to other galaxy properties like stellar mass and the surrounding environment (e.g., Nelson et al. 2018; Wright et al. 2019).

In this work, we focus on the sub-mm dust emission of galaxies within the GV. As highlighted by Eales et al. (2018) using *Herschel* data, GV galaxies display notably strong sub-mm emission compared to galaxies with either bluer or redder optical colors. We explore this characteristic using a galaxy catalog generated from a semi-analytic model (SAM) that includes a self-consistent model of dust formation and evolution. By applying a radiative transfer (RT) approach, we derive observable properties that account for both stellar emission and the absorption and re-emission by dust grains. After defining GV galaxies with a new criterion applicable to any dataset, we find that the number of  $250\ \mu\text{m}$  emitters in the GV is comparable to that found in the BC, in keeping with local observations. This is because, despite a decline in sSFR and the resulting green optical colors, the dust content remains high during the GV phase, fueling the sub-mm emission. The differences in the evolution of sSFR and dust content make sub-mm emission a potential indicator for identifying rejuvenating galaxies, which transition to bluer optical colors while still exhibiting low sub-mm fluxes.

The paper is organized as follows. We introduce our simulated galaxy catalog in Section 2, and in particular the pipeline to obtain observable properties from it (Section 2.2), while the observational data we compare with are presented in Section 3. After inspecting the color–mass diagram predicted by our simulation in Section 4, we present our new definition of GV in Section 5, which is applied to both the simulated and observed sample of galaxies. We then move to analyse dust attenuation in GV galaxies in Section 6, while Section 7 and 8 focus on dust  $250\ \mu\text{m}$  emission. The emission in systems undergoing rejuvenation is discussed in Section 9. Finally, we summarise our results and highlight the main conclusions in Section 10.

## 2. Simulated galaxy catalog

### 2.1. The SAM

We build our catalog of simulated galaxies starting from the L-GALAXIES semi-analytic model (SAM). In particular, we adopt its last public release<sup>1</sup> (Henriques et al. 2020), along with the updates introduced and discussed in Parente et al. (2023). Among these updates, of relevance to this work is the inclusion of a detailed model for the production and evolution of dust grains, inspired to the dust model adopted by our group in hydrodynamic simulations (Granato et al. 2021; Parente et al. 2022). The dust model (see Section 2.1 of Parente et al. 2023 for an exhaustive description) includes two sizes and two chemical compositions of grains. Grains are produced in AGB stars envelopes and type-II SNe ejecta, thus ejected into the surrounding gaseous medium. Different processes are then taken into account, which affect the mass (grains accretion, destruction in SNe shocks, thermal sputtering) and the size (shattering, coagulation) evolution of grains. These processes depend on the physical properties of the galaxy as provided by the SAM (e.g. molecular gas fraction, hot gas temperature, metallicity). The dust content and properties as predicted by the SAM are a crucial ingredient for predicting the observability of simulated galaxies, as detailed in Section 2.2.

The SAM is run on top of the MILLENNIUM merger trees (Springel et al. 2005, box size 500 Mpc/h,  $2160^3$  particles), and a *Planck* cosmology<sup>2</sup> (Planck Collaboration et al. 2014) is assumed throughout this work ( $h = 0.673$ ,  $\Omega_m = 0.315$ ,  $\Omega_b = 0.0487$ ,  $\sigma_8 = 0.829$ ). A Chabrier (2003) initial mass function (IMF) is adopted, with with mass limits  $0.1 - 100 M_\odot$ . We analyse galaxies with a stellar mass content of at least  $\log(M_{\text{stars}}/M_\odot) \geq 9$ , which approximately corresponds to the resolution limit of the underlying DM simulation (e.g. Guo et al. 2011). In this work, to keep the analysis within a reasonable computational time, a reduced sample – preserving the same SMF as the full simulation – is post-processed to derive observable properties.

### 2.2. Radiative Transfer with GRASIL

The observable properties of our simulated galaxies are derived using the Radiative Transfer (RT) code GRASIL (Silva et al. 1998; Granato et al. 2000). This code computes the emission from stellar populations and the absorption and thermal emission from dust grains. It utilises the information on star formation histories (SFHs), the geometry of stars and ISM, and the abundance and properties of dust grains for each galaxy as predicted by the SAM, as detailed in the following sections. We refer to the above-mentioned papers for a detailed description of GRASIL.

#### 2.2.1. Stars and ISM geometry

Simulated galaxies are assumed to have a disc-like interstellar medium (ISM), while the stellar component is organized into a

<sup>1</sup> The source code is available at [https://github.com/LGalaxiesPublicRelease/LGalaxies\\_PublicRepository/releases/tag/Henriques2020](https://github.com/LGalaxiesPublicRelease/LGalaxies_PublicRepository/releases/tag/Henriques2020)

<sup>2</sup> The cosmology originally adopted in the MILLENNIUM simulation has been scaled according to Angulo & White (2010) and Angulo & Hilbert (2015).

disc and a bulge. Both the stellar and ISM discs follow a radial and vertical exponential profile, meaning the density of the disc is given by

$$\rho \propto \exp(-r/r_d) \exp(-|z|/z_d), \quad (1)$$

where  $r$  and  $z$  are the radial and vertical coordinate, while  $r_d$  and  $z_d$  the respective scale lengths of the exponential profiles. The scale length radii of the stellar and ISM discs are predictions from the SAM (note that these values usually differ). For both cases, we set the scale height to 0.1 of the scale radius. The stellar bulge is assumed to have a King profile, with its core radius derived from the half-mass radius predicted by the SAM.

### 2.2.2. Stellar emission

The stellar emission of galaxies originates from the populations in the disc and bulge. Both components have an associated SFH<sup>3</sup>, which tracks the time assembly of their stellar mass and metallicity. The SFH is stored in  $N_{\text{SFH}}$  time bins, with the size of each bin varying with time so that the most recent bins have the highest resolution (see Figure S2 of the Henriques et al. 2020 documentation for a schematic representation). The emission from stellar populations at time  $t$  is calculated (for both disc and bulge stars) by summing over the SFH bins:

$$L(t) = \sum_{i=0}^{N_{\text{SFH}}} l_i(t - t_i; Z_i) \cdot \psi_i \Delta t_i, \quad (2)$$

where  $l_i(t - t_i; Z_i)$  is the emission associated with a unit mass simple stellar population featuring age<sup>4</sup>  $t - t_i$  and metallicity  $Z_i$ ,  $\psi_i$  and  $\Delta t_i$  are the SFR and time width associated with the  $i$ -th bin.

### 2.2.3. Radiative Transfer

Radiation emitted from stars propagates into the ISM, where it is extinguished, heats dust grains, and causes their subsequent thermal emission. Modeling these processes requires detailed RT computations, which are performed by GRASIL.

The interaction between starlight and dust grains depends on the abundance and properties of the latter. The mass of dust in each galaxy, as well as the chemical composition and size of the grains, are predictions of the SAM. Specifically, the model predicts the abundance of four dust species, following two chemical compositions (silicate and carbonaceous) and two sizes with representative radii of  $0.05 \mu\text{m}$  and  $0.005 \mu\text{m}$  (referred to as large and small, respectively). GRASIL uses this information and considers a population of silicate and carbonaceous grains with two different grain size distributions, which are power laws shaped by the ratio of small to large grains. These information are needed to model the absorption and emission of grains.

Dust is assumed to be organized into two phases of the ISM: the dense molecular clouds (MCs) and the diffuse medium. Dust properties are assumed to be the same in the two regions. The fraction of the total dust mass residing in MCs is  $f_{\text{mol}}$ , which is

<sup>3</sup> The same SFH is adopted within the SAM to compute the chemical enrichment from stars. However, although the SFH in the code is recorded on a ring-by-ring basis, for GRASIL post-processing we use the SFH integrated over the entire stellar disc and bulge.

<sup>4</sup> Here  $t_i$  is the central time of the  $i$ -th bin.

the fraction of the total ISM gas in molecular form. This parameter is predicted by the SAM, which relies on the Krumholz et al. (2009) prescription.

MCs are assumed to have a mass  $M_c$  and a radius  $r_c$ , whose combination  $M_c/r_c^2$  is a parameter of GRASIL. This represents the optical depth of the clouds. Stars are assumed to form in these clouds and progressively escape according to an escape timescale  $t_{\text{esc}}$ . Specifically, the fraction of stars inside MCs decreases with time according to

$$f(t) = \begin{cases} 1 & t \leq t_{\text{esc}}, \\ 2 - t/t_{\text{esc}} & t_{\text{esc}} < t \leq 2t_{\text{esc}}, \\ 0 & t > 2t_{\text{esc}}. \end{cases} \quad (3)$$

The escape time  $t_{\text{esc}}$  is a GRASIL parameter and is set to 3 Myr here. Starlight propagation in MCs is simulated using full RT computations (Granato & Danese 1994) because the high densities of these objects make the self-absorption of IR photons significant.

In contrast, starlight propagation in the diffuse medium (where IR photon self-absorption is negligible) is treated in a simplified manner by introducing an *effective* absorption optical depth, defined as  $\tau_{\text{abs,eff}} = \sqrt{\tau_{\text{abs}}(\tau_{\text{abs}} + \tau_{\text{sca}})}$ , where  $\tau_{\text{abs}}$  and  $\tau_{\text{sca}}$  are the *true* absorption and scattering optical depths, respectively.

The outcome of the pipeline described above is that, at each point of the galaxy, stellar radiation is absorbed, the temperature of the grains is calculated (with large grains reaching an equilibrium temperature and small grains experiencing stochastic temperature fluctuations), and the dust emission is modelled as a grey body. This results in a SED from  $0.1 \mu\text{m}$  to  $1000 \mu\text{m}$  for each galaxy along a given line of sight. The apparent magnitude of the galaxy in a specific band is then obtained by convolving the resulting SED with the appropriate filter.

## 3. Observational data

The observational analysis presented in this work relies on data from the Galaxy And Mass Assembly (GAMA) survey<sup>5</sup> (Driver et al. 2009, 2011; Liske et al. 2015; Baldry et al. 2018; Driver et al. 2022). This is a spectroscopic, large scale survey covering a total area of  $\sim 280 \text{ deg}^2$  across five different regions of the sky. Together with spectroscopic redshifts, this survey provides panoramic photometry for  $\geq 200,000$  galaxies obtained combining data from other surveys operating from the X-ray to the FIR side of the spectrum. Moreover, many other data products obtained from SED fitting are available, such as stellar masses, SFRs, dust masses.

In this work we exploit the last GAMA Data Release DR4 (Driver et al. 2022). In particular, we use GAMA II<sup>6</sup> data for the three equatorial survey regions G09, G12 and G15, which all have a limiting Petrosian  $r$ -band apparent magnitude of 19.8. We select galaxies with high quality redshift measurements in the range  $0.002 < z < 0.8$ . In our analysis we are interested in the optical colour  $u - r$  and the sub-mm  $250 \mu\text{m}$  emission of galaxies. GAMA provides both quantities, the former coming from the Sloan Digital Sky Survey (SDSS; Abazajian et al. 2009) and the latter from the  $H$ -ATLAS survey (Eales et al. 2010; Valiante et al. 2016). Here we use the matched aperture photometry fluxes

<sup>5</sup> <https://www.gama-survey.org/>

<sup>6</sup> The second GAMA surveying phase.

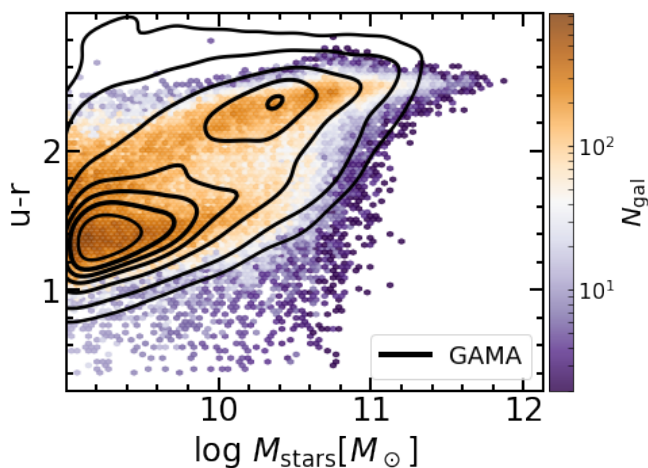


**Fig. 1.** Color ( $u-r$ ) – stellar mass diagram at  $z \leq 0.08$  for our simulated galaxies (2D histogram). Contour lines are 1, 5, 20, 50, 70, 80, 90% of the distribution and refer to the same color–mass relation in the GAMA sample adopted in this work. The  $u-r$  color is dust-attenuated and  $k$ -corrected to  $z = 0$ .

obtained from the LAMBDA<sub>R</sub> code (Wright et al. 2016) and select galaxies with a signal-to-noise ratio  $> 3$ . Fluxes are corrected for galactic extinction and  $k$ -corrected to  $z = 0$  (i.e. they are rest-frame; Loveday et al. 2012). Finally, we use stellar masses obtained from this photometry by SED fitting (Taylor et al. 2011), selecting galaxies with  $M_{\text{stars}} \geq 10^9 M_{\odot}$ , as in our simulated sample.

#### 4. The color–mass diagram

Before analysing any properties of GV galaxies in our catalogs, it is worth looking at the distribution of simulated galaxies in the color–mass diagram. The color ( $u-r$ ) – stellar mass diagram for local galaxies ( $z \leq 0.08$ ) is reported in Figure 1. For comparison, we also report observations from the GAMA sample as black contours. The reported colors are  $k$ -corrected to  $z = 0$  and dust-attenuated, the latter meaning that they are not intrinsic stellar colors.

Our model produces a clear population of blue galaxies at  $M_{\text{stars}} \lesssim 10^{10.5} M_{\odot}$ , which well matches the observed BC. As for red galaxies, in our model these are typically more massive than the blue ones, in line with observations. However, our model overproduces the abundance of low mass ( $M_{\text{stars}} \lesssim 10^{10} M_{\odot}$ ) red galaxies. These are mainly satellite systems, and in particular orphan galaxies. This has been noted recently by Harrold et al. (2024) in the context of L-GALAXIES. These authors highlighted the overabundance of orphans in the low mass SMF at  $0.5 < z < 3$ , and claimed that increasing star formation in these systems could help resolve this problem.

A similar distribution, and similar issues as well, are observed when adopting  $\text{NUV}-r$  or  $g-r$  colors, not shown here for brevity.

#### 5. Defining the GV

The GV lacks a universally accepted definition, with its boundaries differing across studies and often being set by subjective empirical lines. Since our work involves defining the GV in both observed and simulated samples, we aim to establish a clear,

objective definition that can be applied automatically, free from subjective criteria.

##### – Gaussian fits

We adopt a Gaussian fitting approach to define the GV, which applies to any color–mass distribution of galaxies. The sample is first divided into  $N_{\text{bins}}$  mass bins, with only bins containing more than 50 objects being considered. Within each bin, we use the Python class `GaussianMixture` to fit one and two Gaussians to the color distribution. For the two Gaussians fit, this class also provides the mixture *weights* of the resulting Gaussian components, indicating the significance of each component in the overall distribution. Additionally, it computes the Bayesian Information Criterion (BIC) value, which helps balance the trade-off between the goodness of fit and the complexity of the model, favoring models that achieve a good fit with fewer parameters.

We apply three criteria to determine whether the distribution is better represented by one or two populations.

- (i) The BIC value must favour the two Gaussians model.
- (ii) None of the obtained *weights*  $w$  must be less than  $w_{\text{min}} = 0.2$ .
- (ii) The areas within one standard deviation in the two Gaussian curves must not overlap.

When all conditions are met, we determine that the color distribution is described by a two Gaussians fit. The means  $\mu$  and standard deviations  $\sigma$  of these Gaussian components are used to help determine the presence of a GV in the distribution. Specifically, denoting  $x_{\text{BR}}$  as the intersection point of the blue and red Gaussians, we require that

$$\begin{cases} \mu_{\text{R}} - \sigma_{\text{R}} \geq x_{\text{BR}}, \\ \mu_{\text{B}} + \sigma_{\text{B}} \leq x_{\text{BR}}, \end{cases} \quad (4)$$

where the subscripts B and R refer to the blue and red Gaussians, respectively. This approach defines the GV, which we term the real GV, as the region of the color distribution spanning from  $\mu_{\text{B}} + \sigma_{\text{B}}$  to  $\mu_{\text{R}} - \sigma_{\text{R}}$ .

The described conditions at work are explicitly shown in Figure 2, in the left and middle panels. Our algorithm prefers a double-Gaussian fit for the distribution in both mass bins. However, in the  $9 < \log M_{*}/M_{\odot} \leq 9.35$  mass bin, the two Gaussians do not meet the criterion specified in Equation 4, so a *real* GV is not identified. In contrast, the Gaussians in the  $10.05 < \log M_{*}/M_{\odot} \leq 10.40$  bin are well-separated, allowing us to identify a *real* GV, represented by the green distribution in the histogram.

When the algorithm favors a single-Gaussian fit, we proceed as follows. We first identify the peak of the entire distribution and isolate the portion extending from this peak to the nearest extreme. This segment is then mirrored to create a symmetric distribution centered on the original peak. We fit this mirrored distribution with a single Gaussian, using its mean and standard deviation to represent the population.

An example of this process is illustrated in the right panel of Figure 2. The mirrored distribution, shown in dark gray, is fitted with a Gaussian (yellow curve), in contrast to the red curve used to fit the full distribution (light gray). This mirroring technique effectively removes the tail of the distribution, yielding Gaussian parameters that better represent the bulk of the objects in this region.

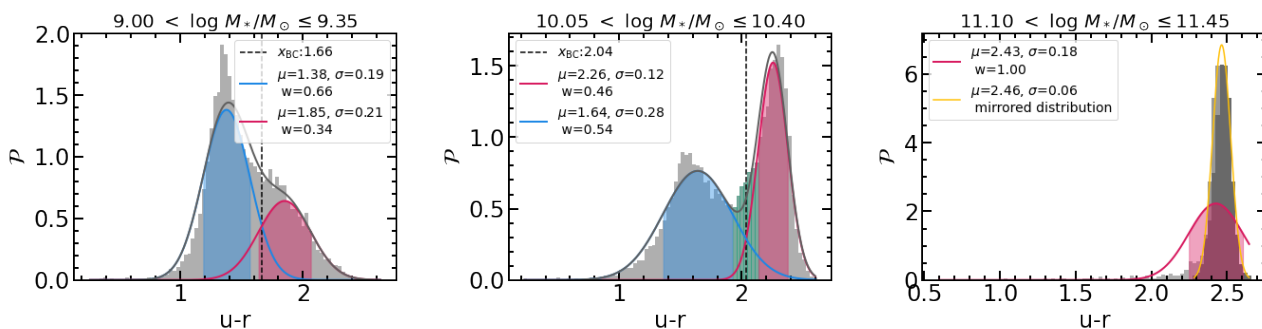


**Fig. 2.** Examples of the Gaussian fits based algorithm used to identify blue and red populations across different mass bins are shown. The three cases illustrate the color distribution of our simulated sample at  $z \leq 0.08$  in three different mass bins, offering a clear demonstration of how our algorithm works (see text for full details). The full color distribution of galaxies in each bin is shown as a gray histogram, and the Gaussian fits are reported as curves, with the shaded regions indicating the standard deviation, and the dashed line the intersection between the two curves (where present). The parameters for each Gaussian (mean  $\mu$ , standard deviation  $\sigma$ , and weight  $w$ ) are labeled in every panel. In the left and middle panels, our algorithm favours a double Gaussian distribution (blue and red, with the gray line indicating their sum). However, a real GV (green histogram) is identified only in the middle panel, since here the condition in Equation 4 is met. In the right panel, the algorithm prefers a single Gaussian fit, which is reported as a red curve. In this case, a subsample of the total is extracted to obtain a symmetric distribution centered around the peak of the original. This sub-distribution, represented by the dark gray histogram, is fitted by the yellow Gaussian curve. The parameters from this fit better represent the red population in this mass bin and are used in our analysis.

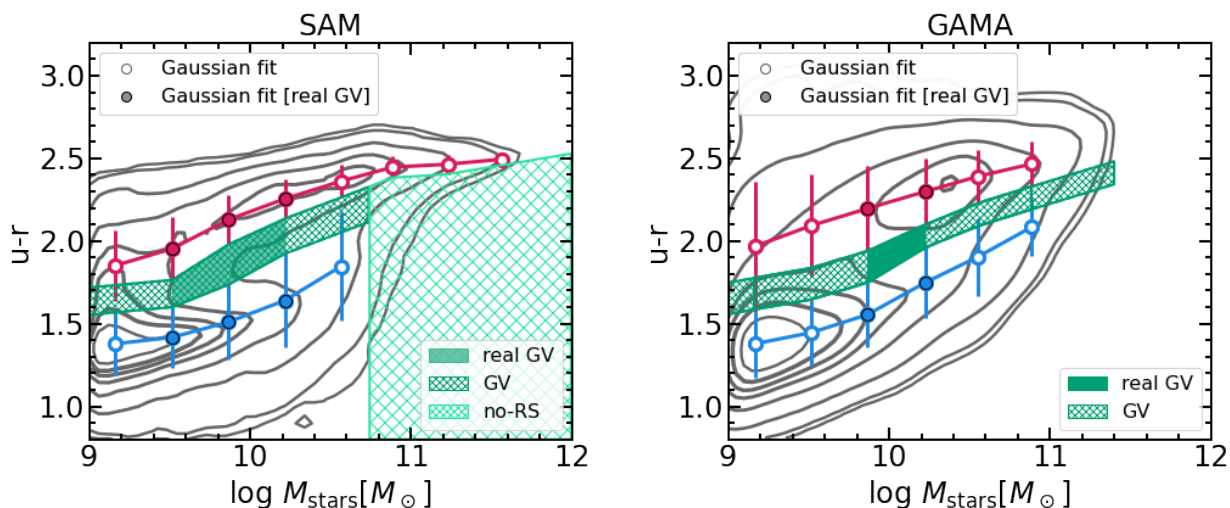


**Fig. 3.** GV identification in the color–mass diagram of both our simulated and observed sample at  $z \leq 0.08$ . The distribution of galaxies is shown as contours marking the 1, 5, 20, 50, 70, 80, 90 % percentiles of the distribution. The circles and error bars indicate the mean and standard deviation of the Gaussian fits performed by our algorithm in each mass bin for both the blue and red population. Filled circles are associated with bins in which the real GV can be identified (according to Equation 4). This region is depicted as solid green in the plots. The green hatched region represents an extension of this GV, obtained by using information from the Gaussian fits. The light green hatched region in the SAM sample marks the region of the diagram where galaxies are identified as *not* belonging to the RS, since a single Gaussian fit is favoured at these mass bins. In the GAMA sample, the GV has been linearly extrapolated in the high stellar mass range where the number of galaxies per bin resulted to be not sufficient to perform a double Gaussian fit ( $< 50$  galaxies).

### – Building the GV

The fitting procedure described above results in the Gaussian function parameters for each mass bin of the distribution. These parameters are then used to split the color–mass diagram into different classes (particularly to identify a GV), as illustrated in Figure 3 for both the simulated and observed samples.

We begin with the real GV, identified in the bins where the condition in Equation 4 is satisfied. In these cases, the GV directly corresponds to the real GV, represented by the green shaded area in Figure 3.

In the mass bins where the algorithm does not identify a real GV but still applies a two Gaussians fit, we extend the real GV by using the Gaussian parameters and assigning a width based

on that of the real GV. Specifically, we select the Gaussian with the highest weight in the double-Gaussian fit. Given the mean and standard deviation of this Gaussian, the extended GV in this mass bin is defined with bounds of  $\mu \pm \sigma$  and  $\mu \pm (\sigma + \Delta_{\text{real,GV}}^{\text{near}})$ , where  $\Delta_{\text{real,GV}}^{\text{near}}$  represents the width of the real GV in the nearest mass bin where it has been identified. If two neighbouring mass bins have a real GV, the average width is used. The  $\pm$  sign is chosen based on the Gaussian fit, with  $+$  for blue and  $-$  for red. This extended GV is shown as a hatched green region in Figure 3. This approach allows us to define a GV in the color–mass diagram for every mass bin where a two Gaussians fit has been applied.

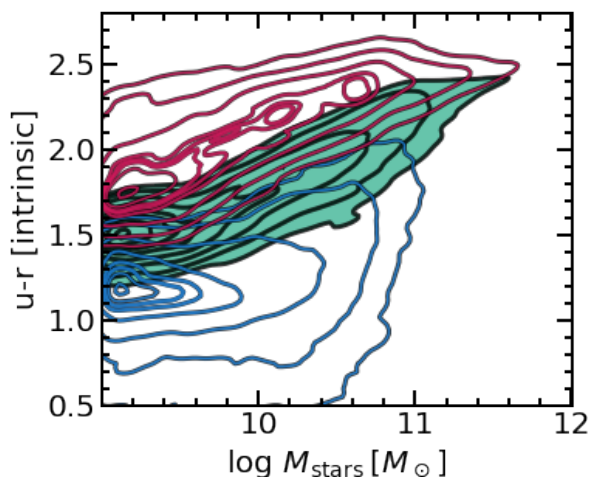


**Fig. 4.** Intrinsic color ( $u - r$ )–mass diagram for our sample of simulated galaxies at  $z \leq 0.08$ . Contour lines represent the 1, 5, 20, 50, 70, 80, 90% of the distribution. Red, green and blue contours refer to galaxies in the RS, GV and BC, respectively, as defined using the dust-attenuated color–mass diagram (Section 5).

In cases where a single-Gaussian fit is used, we take a more conservative approach and choose not to define a GV. Instead, we divide the galaxy population into two categories, using  $\mu \pm \sigma$  as the boundaries for these groups, with  $-$  for a red peak and  $+$  for a blue peak. If a red peak is identified, the categories are labeled RS and no-RS. If a blue peak is identified, they are labeled BC and no-BC. This scenario occurs in the most massive bins of our simulated sample, where only the red population is clearly defined, as indicated in light green in Figure 3. Conversely, in high-redshift snapshots of our simulation, it is more common to find only a clear blue population in the less massive bins (see Figure 8).

This definition allows us to identify a GV (where possible) for any given distribution in the color–mass diagram. Once the GV is specified, the BC and RS are defined as everything below and above the GV, respectively (except in cases where no-BC or no-RS is identified). It is important to note that our approach is fairly conservative, as we avoid extrapolating the GV to mass bins where a clear colour bimodality is not observed. However, our findings remain largely unaffected by this definition. We have verified that using alternative methods, such as extrapolating the GV where a single Gaussian is preferred or applying two simple linear fits to delimit the GV, would not significantly alter our conclusions.

All analyses presented below use the GV definition outlined above, specifically the region formed by the real GV and its extensions, where a two Gaussians fit is preferred.

## 6. The impact of dust attenuation

It is well known that dust obscuration reddens the true, *intrinsic* color of galaxies resulting from stellar emission. Consequently, some intrinsically blue, star-forming galaxies may appear redder (green or red in our classification). We exploit our simulated sample, for which both dust-attenuated and dust-free colors are available, to explore the impact of dust on shaping the color–mass diagram.

In our model, the BC and GV galaxies typically have more dust than equal-mass galaxies in the RS, which are mainly pas-

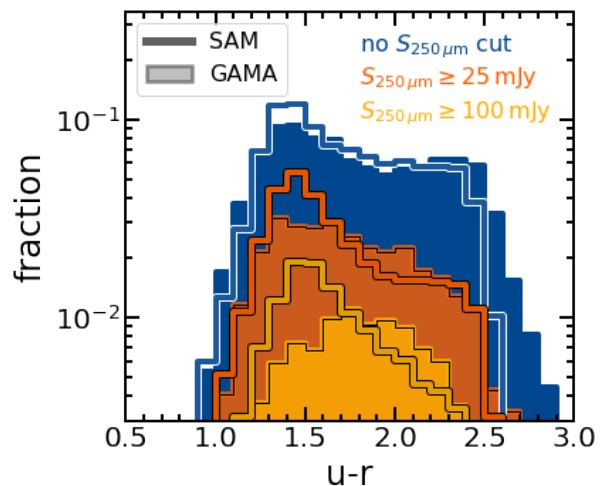


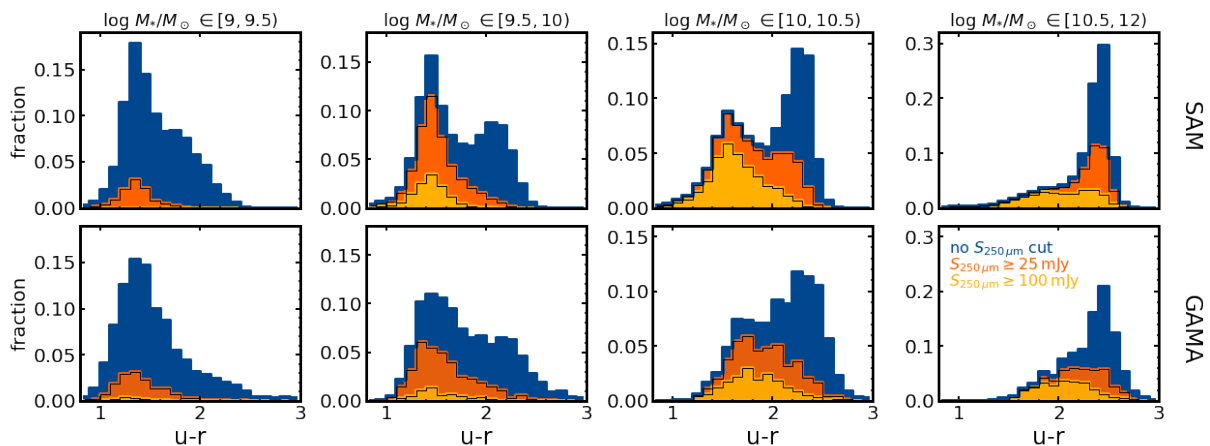
**Fig. 5.** Color  $u - r$  distribution for all the galaxies in both our simulated (solid lines) and observed sample (filled histograms) at  $z \leq 0.08$ . We report the full-colour distribution in dark blue and the one obtained when selecting galaxies with a  $S_{250\mu\text{m}}$  larger than a given threshold, i.e. 25 and 100 mJy (orange and yellow).

sive and gas-poor. As a result, dust reddening is more pronounced for galaxies in the BC and GV, where the intrinsic  $u - r$  color is reddened by  $\sim 0.4 - 0.2$  dex. Attenuation is modest in RS galaxies ( $\lesssim 0.2 - 0.1$  dex).

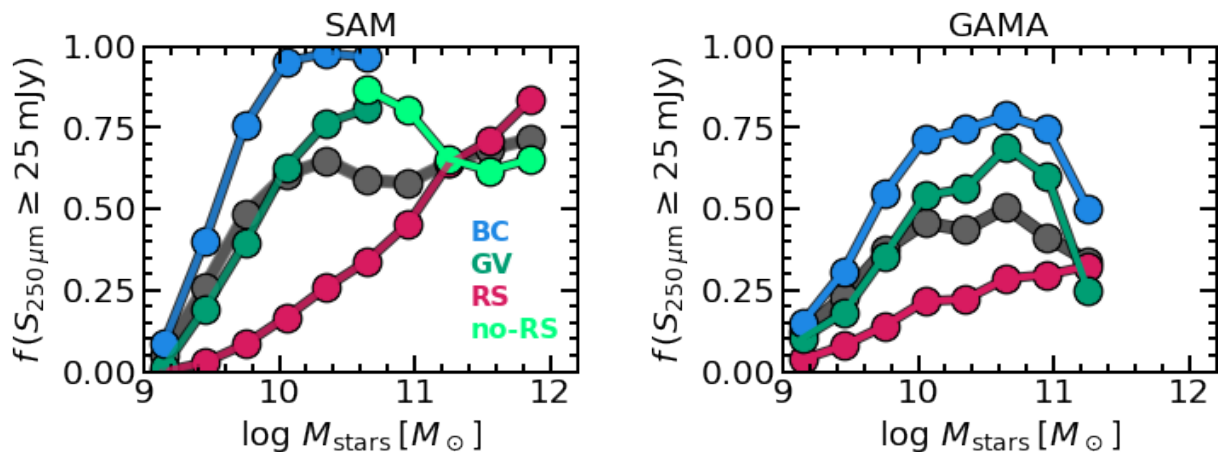
In light of this, when considering intrinsic colors the blue region of the color–mass diagram shifts downward by about  $0.2 - 0.3$  dex, while intrinsic colors are nearly identical to dust-attenuated ones for red galaxies. The net effect of the attenuated-to-intrinsic transformation is a shift towards bluer  $u - r$  colors, which is more pronounced for blue galaxies. Importantly, in this transformation, GV galaxies likely remain GV galaxies: although their color becomes bluer, most dust-attenuated GV galaxies also have intrinsic green colors. In other words, the transition population identified in the dust-attenuated color–mass diagram of Figure 1 mainly consists of galaxies with intrinsic intermediate colors. The percentage of significant outliers due to dust attenuation is very low. To give an idea, only  $\sim 6.5\%$  of intrinsically blue galaxies move to the GV when dust attenuation is considered. As for the transformation of the GV, the  $\sim 94\%$  of galaxies belonging to the intrinsic GV are within  $0.2$  dex of the dust-attenuated GV. These percentages were derived by defining BC, GV, and RS in the intrinsic color–mass diagram using the same procedure detailed in Section 5 for the dust-attenuated diagram.

Figure 4 further illustrates the modest impact of dust on the RS/GV/BC classification. Keeping the categories established in Figure 3, we now plot the intrinsic colour of galaxies on the y-axis. The contours overlap illustrates the extent to which colors shift due to dust attenuation. The bulk of the GV population is observed to have intermediate intrinsic colors.

This analysis concludes that although dust obscuration plays a role in reddening galaxies, the bulk of the galaxies in a dust-attenuated GV belong to a transition region in the intrinsic color–mass diagram.



**Fig. 6.** Color distribution in different stellar mass bins for our model (top panels) and observed (bottom panels) galaxies at  $z \leq 0.08$ . In each panel we report the total distribution (dark blue histograms), as well as the distribution obtained applying different cuts on the  $250\mu\text{m}$  flux, namely  $S_{250\mu\text{m}} \geq 25$  and  $100$  mJy (respectively orange and yellow histograms).



**Fig. 7.** Fraction of galaxies in the BC (blue), GV (green) and RS (red) with a  $S_{250\mu\text{m}}$  flux larger than  $25$  mJy as a function of stellar mass in both our model (left) and GAMA sample (right panel). The left sample (SAM) also includes galaxies classified as *not* belonging to the RS in light green (no-RS; see Section 5). Results for the whole samples are reported in gray.

## 7. The sub-mm $250\mu\text{m}$ emission

In this Section we analyse the sub-mm  $250\mu\text{m}$  emission of both simulated and observed  $z \leq 0.08$  galaxies. We start from the  $u-r$  color distribution as reported in Figure 5, imposing a threshold ( $25$  or  $100$  mJy) on  $S_{250\mu\text{m}}$ . The  $25$  mJy threshold, which will be adopted in the rest of this work, is approximately the flux value of the 14th percentile of the observed  $S_{250\mu\text{m}}$  distribution when selecting objects with a signal-to-noise ratio larger than  $3$ . For this reason, we will often refer to the objects satisfying this criterion as sub-mm emitters.

In model galaxies, both the  $S_{250\mu\text{m}} \geq 25$  mJy and  $S_{250\mu\text{m}} \geq 100$  mJy distributions are biased towards the blue peak, indicating that blue galaxies are more likely to have significant sub-mm emissions. This is also the case for the  $S_{250\mu\text{m}} \geq 25$  mJy distribution of the GAMA sample. However, when raising the sub-mm emission threshold to  $100$  mJy, the distribution of observed galaxies peaks at around intermediate colors.

A similar result was previously noted by Eales et al. (2018), based on a similar dataset<sup>7</sup>. They observed that sub-mm detected galaxies (specifically those with  $250\mu\text{m}$  emission  $\geq 30$  mJy from  $H$ -ATLAS) are predominantly located in the optical GV. They suggested that this could originate from a continuous, *non*-bimodal distribution of galaxies in the  $M_{\text{stars}}$ -SFR diagram, attributing the SFR bimodality to an incorrect mapping between colors and SFR (and vice versa). In other words, they interpret the observation of a "green mountain" as an argument against the widely accepted scenario which associate GV galaxies to a transition (in terms of SFR) population. While we stay agnostic regarding this conclusion, we will exploit our model to investigate the substantial sub-mm emission in GV galaxies.

We conduct a more detailed analysis of the above result, noting that in general color distributions shift towards redder colors with increasing stellar mass (e.g. Figure 1). We perform the

<sup>7</sup> We have exploited more recent data products of the GAMA team, particularly matched aperture photometry. Also, our limiting  $250\mu\text{m}$  fluxes are different.

same analysis by splitting the samples into various mass bins, as shown in Figure 6. At fixed stellar mass, galaxies with bluer colors have a higher fraction of sub-mm emitters. Thus, the analysis reveals that  $S_{250\mu\text{m}}$  emission is likely present in galaxies with colors within the blue peak of the  $u - r$  distribution, as well as within the GV region between the blue and red peaks. This finding is consistent in both the simulated and observed samples.

This analysis helps to understand the main discrepancy between our model galaxies and the GAMA sample, as noted in Figure 5, i.e. the different color distribution of  $S_{250\mu\text{m}} \geq 100$  mJy galaxies. Our model produces a non-negligible number of blue,  $S_{250\mu\text{m}} \geq 100$  mJy galaxies with masses  $10 \leq \log M_{\text{stars}}/M_{\odot} < 10.5$ , whereas the GAMA sample shows a lower fraction of blue galaxies in this mass range, with the observed population peaking at redder colors compared to our model predictions. We argue that the primary shortcoming of our model is the overproduction of blue galaxies in this mass range rather than an issue with the sub-mm emission itself. Indeed, when plotting Figure 5 for  $\log M_{\text{stars}}/M_{\odot} < 10$  galaxies (not shown here for brevity), the distribution of  $S_{250\mu\text{m}} \geq 25$  mJy and  $S_{250\mu\text{m}} \geq 100$  mJy galaxies peaks on the blue peak in both the observed and simulated sample.

The above considerations do not rely on any specific definition of the GV but are solely derived from the positions of the blue and red peaks in the color distribution. We can further analyze the results using the explicit definitions of BC, GV, and RS. To accomplish this, we categorize galaxies into these three classes (and also no-RS galaxies for the simulated sample) in both the model and observed samples, as detailed in Section 5.

Figure 7 shows the fraction of galaxies with a  $250\mu\text{m}$  flux larger than 25 mJy as a function of stellar mass for both our model and observations. Across the whole sample (grey points), the fraction of galaxies with  $S_{250\mu\text{m}} \geq 25$  mJy generally increases with stellar mass up to  $M_{\text{stars}} \approx 10^{10} - 10^{11} M_{\odot}$ , after which the slope becomes shallower. The  $250\mu\text{m}$  emission is strongly correlated with the dust content of galaxies. Indeed, this trend mirrors the  $M_{\text{stars}} - M_{\text{dust}}$  relation, which also flattens above a similar stellar mass (e.g., Beeston et al. 2018 for GAMA and Parente et al. 2023 for our model galaxies). This is because galaxies in this stellar mass range have relatively low quantities of gas (and dust) due to the quenching process. In our model, this is regulated by radio-mode AGN feedback.

We also note that the  $f(S_{250\mu\text{m}} \geq 25 \text{ mJy})$  fraction is typically higher in our model by a modest factor compared to GAMA. This is due to slightly larger dust content in intermediate-mass galaxies in our model sample, which is linked with the overproduction of blue, intermediate-mass galaxies in our model as noted above.

A more intriguing insight comes from the analysis of  $f(S_{250\mu\text{m}} \geq 25 \text{ mJy})$  for the different considered populations. In both the model and observed samples, BC and GV galaxies with  $M_{\text{stars}}/M_{\odot} \lesssim 10^{11}$  are more likely to have  $S_{250\mu\text{m}} \geq 25$  mJy, while the fraction is generally lower for RS galaxies. At large stellar masses ( $M_{\text{stars}} \gtrsim 10^{11} M_{\odot}$ ), the differences among the classes reduce. In our model, this behaviour is due to the large fraction of rejuvenating galaxies in this mass range. These galaxies are those that were previously passive (i.e. they were in the RS), but now have bluer colors (meaning that they belong to the no-RS class, since a BC is not explicitly identified in this mass range) as a consequence of a rejuvenation event (a starburst). Despite featuring blue-to-green colors, these rejuvenating systems have relatively low  $250\mu\text{m}$  emission (see discussion in Section 9), lowering the fraction of galaxies with

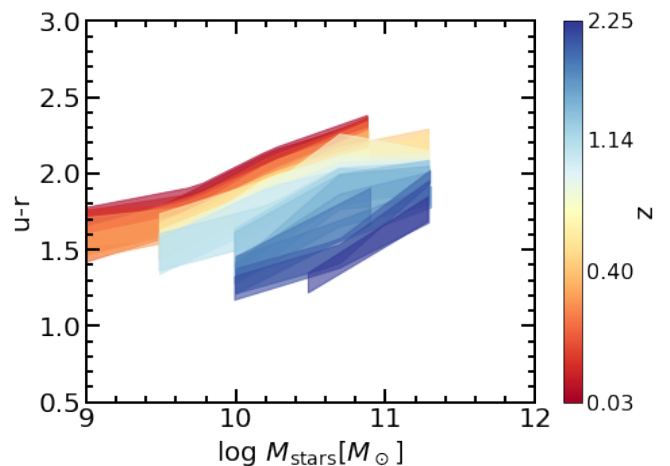


**Fig. 8.** GV evolution with redshift ( $0.03 \leq z \leq 2.25$ ) as identified in our simulation with the method described in Section 5.

$S_{250\mu\text{m}} \geq 25$  mJy.

To conclude this Section, we highlight that our results are independent of the 25 mJy threshold, as the same qualitative behaviour is observed with higher thresholds, such as 50 mJy or 100 mJy. While the adopted GV definition provides a quantitative, albeit approximate, understanding of the sub-mm properties of different populations, we stress that the main result of this Section is independent of the GV definition. The result is that observed and simulated galaxies in both the blue peak and the transitioning region of the color ( $u - r$ ) distribution exhibit substantial sub-mm emission, in contrast to those in the red peak.

## 8. Evolution in the color- $S_{250\mu\text{m}}$ diagram

This Section is devoted to carefully examining the sub-mm emission during the evolution of our model galaxies, with particular focus on the GV phase. It might be argued that the substantial sub-mm emission in GV galaxies occurs because these are fundamentally blue galaxies (i.e., star-forming galaxies) with a significant amount of dust, which reddens their optical colors and fuels the sub-mm emission. However, this is not the case, as already indicated in Section 6 (Figure 4): only  $\sim 6.5\%$  of blue galaxies move to the GV as a result of dust attenuation. Model galaxies in the GV (on average) exhibit intermediate sSFR and intrinsic color, suggesting that they represent a transitioning population rather than merely a dust-reddened one.

The reason for the sub-mm emission of GV galaxies is that, while these galaxies experience a rapid quenching that quickly reduces their sSFR and turns their color green, the amount of dust in these objects remains relatively high, enabling a conspicuous  $250\mu\text{m}$  emission. We will show this comprehensively in the following sections.

### 8.1. Model GV redshift evolution

Since we are interested in the evolution of the properties of our model galaxies, we need to adopt an evolving definition of the GV, which is expected to vary with redshift. We exploit the definition of GV introduced in Section 5 in order to identify it in all the snapshots of our simulations. We only use  $z \leq 2.25$  outputs, but this choice does not impact our results given the young age of the Universe at this redshift. The GV(s) are reported as shaded

regions with different redshift-dependent colors in Figure 8. The two key features to note are the mass and color evolution of these regions. The masses where a GV is identified by our method are generally large at high- $z$ , while they cover nearly the whole range as the redshift decreases. This is because the RS is clearly identified only in the large mass range at high- $z$ . Our method identifies a BC and a no-BC region in the low mass range. Also, we note that the color of the GV progressively becomes redder as the redshift decreases, mirroring the color evolution of the blue and red populations, both bluer at high- $z$ .

### 8.2. A red galaxy case study

We begin by analyzing the evolution of a red galaxy at  $z \simeq 0$ , with  $M_{\text{stars}}^{z=0} \simeq 10^{10.9} M_{\odot}$ . This is illustrated in Figure 9, which shows the evolution of the sSFR, the dust-to-stellar mass ratio ( $M_{\text{dust}}/M_{\text{stars}}$ ), the color ( $u-r$ ), and the  $250\mu\text{m}$  emission. For the latter, we use  $S_{250\mu\text{m}}^{z=0.1}$ , which is  $S_{250\mu\text{m}}$  calculated assuming the galaxy is at  $z = 0.1$  at each time. This particular galaxy was selected because its evolution is relatively smooth in terms of star formation, aside from a few bursty episodes, making it an ideal example for pedagogical purposes. The galaxy is classified as part of the BC, GV or RS, represented by blue, green, and red points based on the redshift-dependent definition of the GV outlined in Section 8.1.

The sSFR of the galaxy gradually decreases, leading to a reddening of its color. Around  $t_{\text{lookback}} \simeq 10$  and  $9$  Gyr, the galaxy transitions into the GV and eventually the RS. The key point to emphasize is that during this transition from the BC to the RS, the galaxy color reddens significantly, while  $S_{250\mu\text{m}}^{z=0.1}$ , though decreasing, remains comparable to its high levels during the BC phase. In other words, while the  $u-r$  color evolves rapidly and consistently towards redder values, the  $S_{250\mu\text{m}}^{z=0.1}$  in the transition (GV) region stays relatively high. This results in a semi-circular trajectory in the color- $S_{250\mu\text{m}}^{z=0.1}$  diagram, where the GV region is characterized by intermediate colors and high  $250\mu\text{m}$  fluxes. This pattern is also reflected in other galaxy properties, particularly dust content and SFR, both normalized to stellar mass. Although the sSFR consistently decreases, the specific dust mass in the GV region remains quite high ( $M_{\text{dust}}/M_{\text{stars}} \gtrsim 10^{-3}$ ), comparable to the values observed during the blue phase.

As the galaxy becomes redder, its  $S_{250\mu\text{m}}$  continues to decline, along with its specific dust mass. During this phase, two noteworthy events occur at  $t_{\text{lookback}} \simeq 5$  and  $8$  Gyr, when the galaxy experiences two bursts of star formation. Each burst temporarily makes the galaxy bluer, moving it from the RS back to the BC for a single snapshot. We refer to galaxies undergoing these events as rejuvenated. However, during these rejuvenation-induced BC phases, the  $S_{250\mu\text{m}}$  remains quite low because the dust production has not had sufficient time to accumulate enough mass to produce significant  $250\mu\text{m}$  emission. We will discuss some interesting implications of this in Section 9 concerning rejuvenating systems.

### 8.3. A red statistical sample

We now turn to the analysis of the evolution of the same key quantities in a large statistical sample of  $\sim 2,000$  red galaxies at  $z \simeq 0$ , namely, the sSFR, dust mass, ( $u-r$ ) color, and  $S_{250\mu\text{m}}^{z=0.1}$ , and are shown in Figure 10. This analysis, averaged over the entire sample, highlights the key features relevant for interpreting the sub-mm flux during the GV transition.

Both the sSFR and ( $u-r$ ) color evolve monotonically towards a passive (or red) state. However, this is not the case for the dust content (and specific dust content), which reaches a maximum at  $t_{\text{lookback}} \sim 9$  Gyr. Notably, this peak does not coincide with the peak in the SFR, which occurs earlier at  $t_{\text{lookback}} \sim 11$  Gyr. This discrepancy is due to two main factors. First, once dust is produced by stars, it remains in the ISM until it is removed by other processes such as astration, galactic outflows, or destruction by SNe. On the contrary, the SFR is an instantaneous quantity, meaning that it keeps track of a relatively short period of the evolution of the galaxy. Second, and more importantly, the dust budget can increase due to grain growth in the ISM, leading to a delay of  $\gtrsim 1$  Gyr between the SFR peak and the dust abundance peak.

Another way to examine this is by comparing the  $e$ -folding decay timescales of the sSFR and dust abundance, as shown in Figure 10. The timescale for dust abundance is roughly twice as long as that for sSFR, indicating a slower decline in dust content.

As a result, the sub-mm  $S_{250\mu\text{m}}$  emission remains relatively high throughout the GV transition due to the large dust content. This is clearly illustrated in Figure 11, where the time-averaged  $S_{250\mu\text{m}}^{z=0.1}$  flux is shown for each of the BC, GV, and RS phases. These values are normalized to the maximum  $250\mu\text{m}$  flux achieved during the evolution of each galaxy. The analysis reveals that, on average, the sub-mm flux during the BC and GV phases is close to the peak flux reached by the galaxies. Median values for the BC and GV phases are  $\sim 42\%$  and  $\sim 40\%$  of the maximum, respectively. In contrast, the mean flux during the red phase is significantly lower,  $\lesssim 15\%$  of the maximum.

### 8.4. The color- $S_{250\mu\text{m}}$ diagram

To conclude, we show the color- $S_{250\mu\text{m}}$  diagram for our model galaxies at  $z \leq 0.08$  in Figure 12. Building on the previous analysis of evolutionary trends, we depict a schematic evolution path in this diagram using a yellow arrow. The key message is that sub-mm emission increases during the BC phase, remains high throughout the GV transition, and then decreases once the galaxy evolves into the RS. Indeed, most red galaxies fall significantly below the  $25$  mJy threshold used here to select sub-mm emitters.

## 9. Rejuvenating systems

The differential variation in color and sub-mm flux has important implications for rejuvenating systems within the GV. Not all galaxies in the GV come directly from the BC. Some of them are undergoing a rejuvenation process, marked by a reverse quenching scenario in which galaxies shift from a quiescent to a star-forming state, often driven by factors such as increased gas supply, which is frequently the result of mergers in our SAM.

In Figure 13 (*left panel*), we show the predicted  $S_{250\mu\text{m}}^{z=0.1}$  as a function of stellar mass for  $z \simeq 0$  galaxies in the GV. We differentiate between quenching GV galaxies and rejuvenating systems transitioning back from the RS to the GV. Rejuvenating galaxies are operationally defined as those that spent at least 3 out of 5 snapshots in the RS just before moving to the GV. While this definition can be somewhat ambiguous due to the episodic nature of star formation and color evolution, it helps identify galaxies that are not simply transitioning from a star-forming state. However, we have also verified that alternative plausible definitions<sup>8</sup>

<sup>8</sup> These include considering galaxies that, just before moving to the GV, have spent (i) at least 5 out of 10 snapshots in the RS, and (ii) 3 consecutive snapshots in the RS.

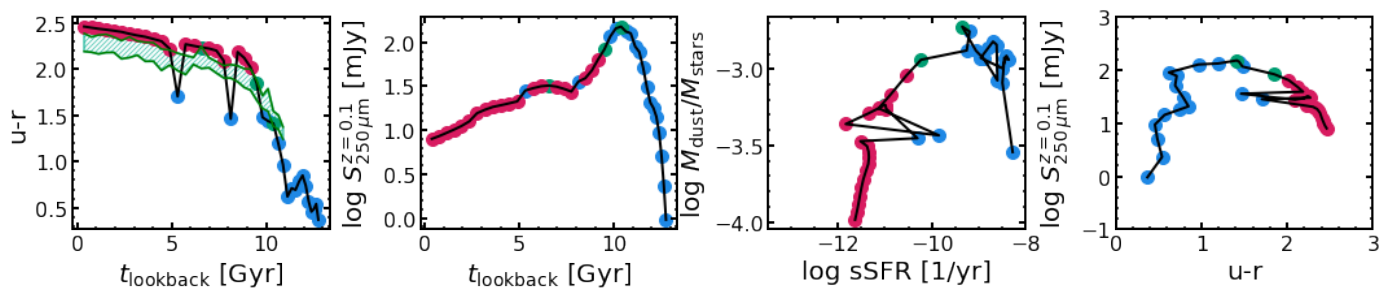


**Fig. 9.** Evolution of a  $z \approx 0$  red sequence galaxy with  $M_{\text{stars}}^{z=0} \approx 10^{10.9} M_{\odot}$ . The top panels display the rest-frame color ( $u-r$ ) evolution and the  $S_{250\mu\text{m}}^{z=0.1}$ . The bottom panels illustrate the evolution of the galaxy in the  $\text{sSFR}-M_{\text{dust}}/M_{\text{stars}}$  and color- $S_{250\mu\text{m}}^{z=0.1}$  diagrams. Each point corresponds to a snapshot of the simulation and is colored accordingly to the galaxy position at that given time in the  $M_{\text{stars}}-S_{250\mu\text{m}}^{z=0.1}$  color diagram (i.e., blue, green, or red for the BC, GV, or RS, respectively) according to the  $z$ -dependent GV definition given in Section 8.1. The reference GV evolution is shown in the first panel.

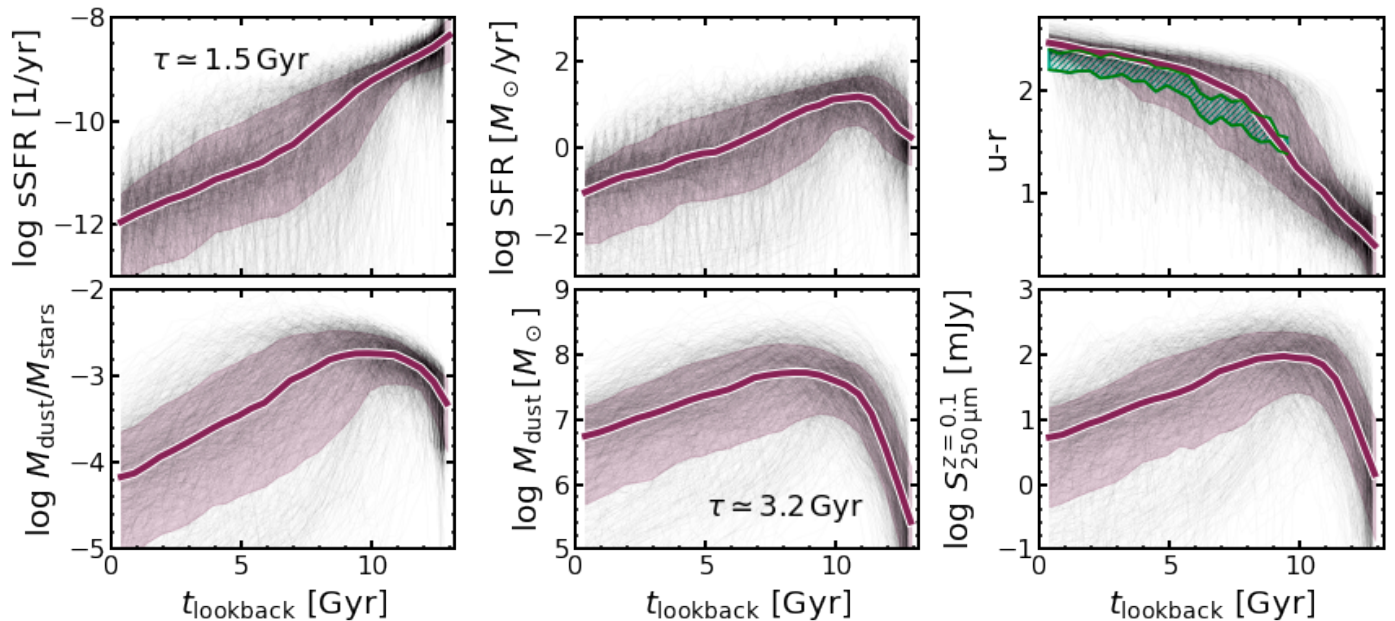


**Fig. 10.** Time evolution of some key quantities for a sample of  $z \sim 0$  red galaxies. In a clockwise order, we show the sSFR, SFR, color  $u-r$ ,  $S_{250\mu\text{m}}^{z=0.1}$  flux, dust mass and specific dust mass. An evolving GV (assuming the median mass evolution of the sample) is shown in the  $(u-r) - \text{time}$  plot. Tracks of individual galaxies in each diagram are shown in gray lines, while we report the median and 16 – 84th percentiles dispersion of all the tracks in red. Finally, we report the typical  $e$ -folding timescales associated to the (decaying) evolution of the sSFR and dust mass.

of rejuvenating galaxies yield similar results. Typically, rejuvenating systems have  $S_{250\mu\text{m}}$  values lower than the GV average. As previously discussed in Section 8.2, this occurs because rejuvenating systems experience bursts of star formation that temporarily make their colors bluer, but they maintain relatively low dust masses, leading to lower  $250\mu\text{m}$  emission.

In the *right panel* of the same figure, we present the distribution of  $S_{250\mu\text{m}}^{z=0.1}$ , normalized to the mean  $S_{250\mu\text{m}}^{z=0.1}$  for each galaxy (averaged over its entire evolution). Rejuvenating systems show lower  $S_{250\mu\text{m}}^{z=0.1}$  fluxes than standard GV galaxies, typically by a median factor of  $\approx 2$ .

In summary, sub-mm emission is a valuable indicator for identifying rejuvenating systems within the GV. Although these systems have green colors similar to other GV galaxies, their sub-mm flux is on average lower, due to their shorter time available to rebuild their dust content.

## 10. Discussion and Conclusions

In this work we have studied the  $250\mu\text{m}$  sub-mm emission of galaxies during their transition through the GV. We utilized predictions from a SAM of galaxy evolution that incorporates processes for the formation and evolution of dust grains within a galactic context. These predictions were employed to estimate observable properties of galaxies, including sub-mm emission, using the radiative transfer code GRASIL, which simulates both dust attenuation and thermal emission of dust grains.

We concentrate on galaxies at  $z \leq 0.08$ , whose distribution in the  $u-r$  color-mass diagram (Figure 1) aligns well with GAMA observations, showing a clear color bimodality, although some tensions are highlighted, especially at low and large stellar masses. To analyze the properties of galaxies in the GV, we introduce a new, precise GV definition that can be applied to any color-mass diagram distribution (Section 5). This allows us to consistently compare our simulation results and observational

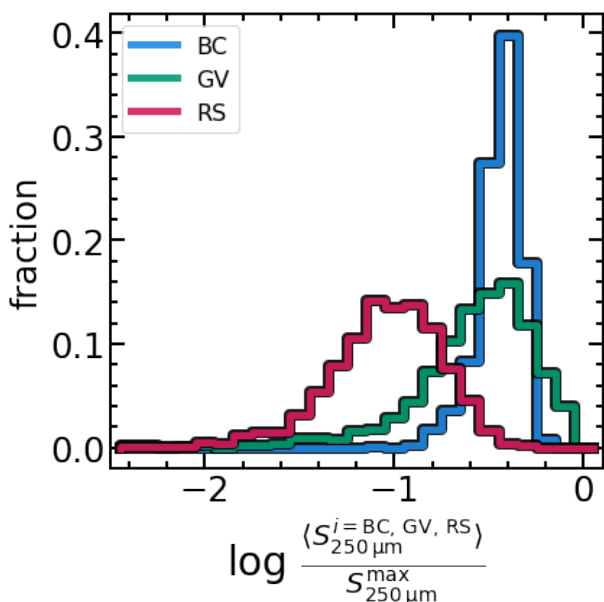


**Fig. 11.** Time averaged  $S_{250\mu\text{m}}^{z=0.1}$  flux normalized to the maximum flux reached during the evolution of each galaxy when it was in the BC, GV, or RS (represented by blue, green, and red histograms, respectively). To construct the histogram, the evolution of the  $S_{250\mu\text{m}}^{z=0.1}$  flux was analyzed for each galaxy in a sample of  $\sim 2,000$  red galaxies at  $z \approx 0$ , and the BC/GV/RS classification was performed according to the redshift evolving GV definition detailed in Section 8.1. For each galaxy, a time averaged  $S_{250\mu\text{m}}^{z=0.1}$  flux was derived for each phase (BC/GV/RS) and then normalized to the maximum  $S_{250\mu\text{m}}^{z=0.1}$  reached.

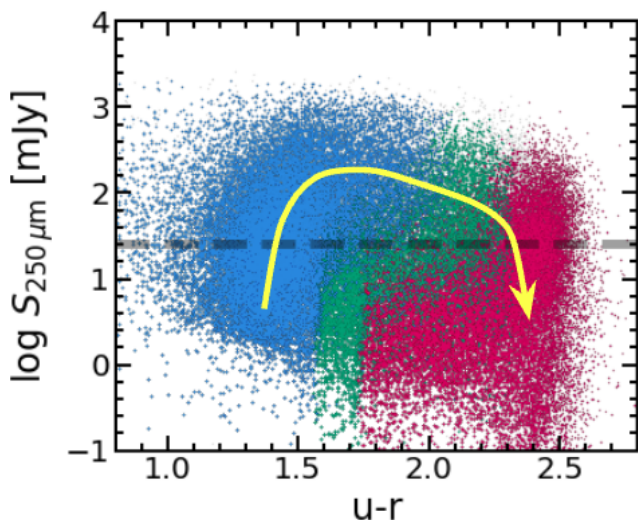


**Fig. 12.** Color- $S_{250\mu\text{m}}$  diagram for our  $z \leq 0.08$  model galaxies in the BC, GV, and RS (represented by blue, green, and red points, respectively). The dashed black line represents the 25 mJy threshold adopted in this work to define sub-mm emitters. The yellow arrow schematically represents the (standard) evolution of a sub-mm bright galaxy in this diagram.

data, although there is no perfect match in terms of absolute colors.

With our new definition, we analyzed various properties of the different galaxy populations identified in the color–mass diagram, mainly the BC, GV and RS. We found that dust-induced attenuation does not significantly alter the distribution of our

model galaxies in this diagram (Figure 4). Galaxies in the GV, as seen in the dust-attenuated color–mass diagram, are generally also identified as transitioning galaxies in a dust-free (or intrinsic) color–mass diagram.

When examining sub-mm emission across different populations, we observed that the BC and GV host a substantial number of sub-mm emitters, defined as those with  $250\mu\text{m}$  emission exceeding 25 mJy. This is true for our simulated galaxy sample and GAMA observations (Figure 7). In contrast, galaxies in the RS exhibit a lower-than-average fraction of sub-mm emitters in both samples. These differences are in place for stellar masses of  $\log M_{\text{stars}}/M_{\odot} \lesssim 10^{11}$ . At higher stellar masses, the fraction of sub-mm emitters is similar across the various populations. We interpret this finding in the context of the numerous rejuvenating systems outside the RS in this mass range, which have blue/green colors but relatively low sub-mm emission.

We use our model to further investigate the sub-mm emission of galaxies during the GV phase. The sSFR of galaxies evolves (on average) in a generally monotonic fashion, causing their color to gradually redden. In contrast,  $250\mu\text{m}$  emission – which is associated with the dust content in galaxies – increases during the BC phase and remains high as galaxies transition toward the RS, making GV galaxies significant sub-mm emitters (Figure 9 and 10). When averaged over time, the  $S_{250\mu\text{m}}^{z=0.1}$  emission during a single-galaxy evolution is similar in both the BC and GV phases, being  $\sim 4$  times higher than during the RS phase (Figure 11).

Finally, we have highlighted that sub-mm emission can help identify rejuvenating GV galaxies. Specifically, at a given stellar mass, GV galaxies undergoing a rejuvenation event exhibit median  $250\mu\text{m}$  emission that is 0.1 – 0.4 dex lower compared to standard GV galaxies (Figure 13). This lower emission is because rejuvenating galaxies become bluer due to a starburst, not having had sufficient time to accumulate enough dust to produce significant sub-mm emission. Testing this prediction on an observed sample, along with other techniques for identifying rejuvenating systems, would be extremely interesting. To refine our understanding of the nature of transition galaxies, in subsequent works, we will extend our multi-wavelength analyses incorporating radio data that could offer a more complete view of the interplay between dust build-up, star formation histories and sub-mm/radio emission in these systems (e.g. Bressan et al. 2002).

In conclusion, we remark the importance of the adopted galaxy evolution model that self-consistently tracks dust formation and evolution, forming the basis of this analysis. The model naturally predicts the delay between star formation and dust content evolution, along with the associated changes in optical colors and sub-mm emission. Moreover, it shows that a high (low) sub-mm emission is not always a safe signature of high (low) star formation activity. GV galaxies in quenching process may still feature a sub-mm similar to those of BC galaxies, while rejuvenating systems, despite being significantly star-forming, may have a relatively low sub-mm emission.

*Acknowledgements.* This project has received funding from the Consejo Nacional de Investigaciones Científicas y Técnicas (CONICET) (PIP-2021-11220200102832CO, PIP-2022-11220210100064CO), from the Agencia Nacional de Promoción de la Investigación, el Desarrollo Tecnológico y la Innovación de la República Argentina (PICT-2018-3743, PICT-2020-3690), from the Secretaría de Ciencia y Tecnología de la Universidad Nacional de Córdoba, and from the European Union’s HORIZON-MSCA-2021-SE-01 Research and Innovation Programme under the Marie Skłodowska-Curie grant agreement number 101086388 - Project LACEGAL.

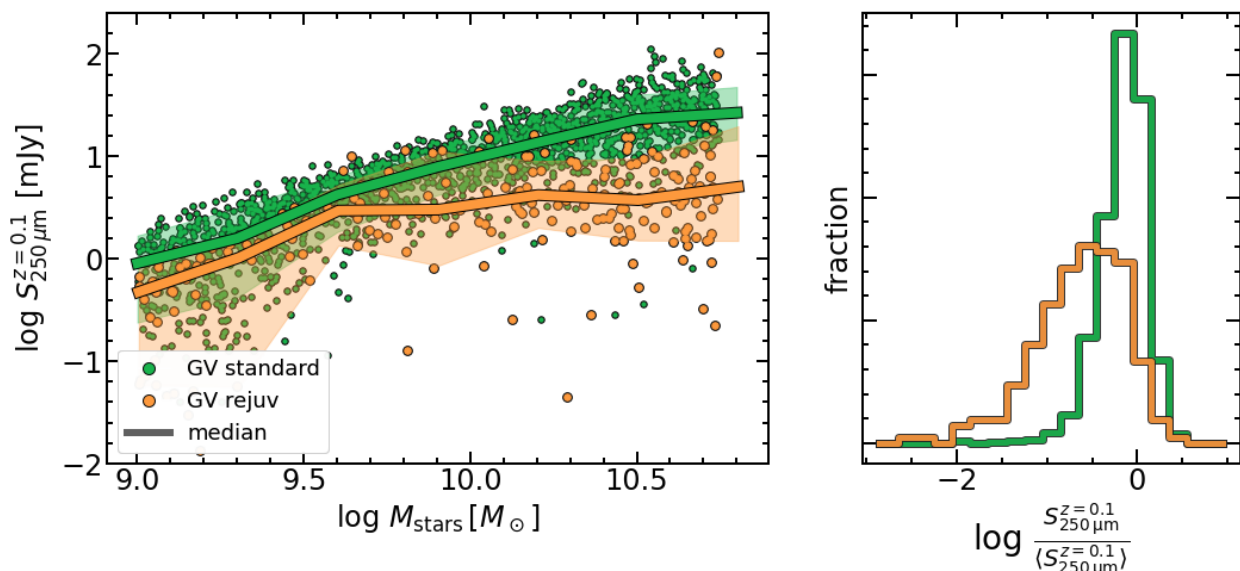


**Fig. 13.** *Left panel:*  $S_{250\mu m}^{z=0.1}$  as a function of stellar mass for  $z \approx 0$  GV galaxies (represented by filled circles). Standard GV galaxies are in green, while rejuvenating systems (transitioning from the RS to the GV) are depicted in orange. Median trends of the two galaxy samples are shown as solid lines, while shaded area refer to the 16 – 84th percentile dispersions. *Right panel:* Distribution of the 250  $\mu m$  flux normalized to the 250  $\mu m$  flux averaged over the entire galaxy evolution for both standard and rejuvenating GV galaxies (green and orange, respectively).

## References

- Abazajian, K. N., Adelman-McCarthy, J. K., Agüeros, M. A., et al. 2009, *ApJS*, 182, 543
- Anghopo, J., Ferreras, I., & Silk, J. 2019, *MNRAS*, 488, L99
- Anghopo, J., Negri, A., Ferreras, I., et al. 2021, *MNRAS*, 502, 3685
- Angulo, R. E. & Hilbert, S. 2015, *MNRAS*, 448, 364
- Angulo, R. E. & White, S. D. M. 2010, *MNRAS*
- Baldry, I. K., Liske, J., Brown, M. J. I., et al. 2018, *MNRAS*, 474, 3875
- Beeston, R. A., Wright, A. H., Maddox, S., et al. 2018, *MNRAS*, 479, 1077
- Blank, M., Macciò, A. V., Kang, X., Dixon, K. L., & Soliman, N. H. 2022, *MNRAS*, 514, 5296
- Bluck, A. F. L., Maiolino, R., Sánchez, S. F., et al. 2020, *MNRAS*, 492, 96
- Bower, R. G., Benson, A. J., & Crain, R. A. 2012, *MNRAS*, 422, 2816
- Brammer, G. B., Whitaker, K. E., van Dokkum, P. G., et al. 2009, *ApJ*, 706, L173
- Bressan, A., Silva, L., & Granato, G. L. 2002, *A&A*, 392, 377
- Chabrier, G. 2003, *PASP*, 115, 763
- Chang, W., Fang, G., Gu, Y., et al. 2022, *ApJ*, 936, 47
- Chauke, P., van der Wel, A., Pacifici, C., et al. 2019, *ApJ*, 877, 48
- Cimatti, A., Brusa, M., Talia, M., et al. 2013, *ApJ*, 779, L13
- Coenda, V., Martínez, H. J., & Muriel, H. 2018, *MNRAS*, 473, 5617
- Dalla Vecchia, C. & Schaye, J. 2008, *MNRAS*, 387, 1431
- Di Matteo, T., Springel, V., & Hernquist, L. 2005, *Nature*, 433, 604
- Driver, S. P., Bellstedt, S., Robotham, A. S. G., et al. 2022, *MNRAS*, 513, 439
- Driver, S. P., Hill, D. T., Kelvin, L. S., et al. 2011, *MNRAS*, 413, 971
- Driver, S. P., Norberg, P., Baldry, I. K., et al. 2009, *Astronomy and Geophysics*, 50, 5.12
- Eales, S., Dunne, L., Clements, D., et al. 2010, *PASP*, 122, 499
- Eales, S. A., Baes, M., Bourne, N., et al. 2018, *MNRAS*, 481, 1183
- González Delgado, R. M., Rodríguez-Martín, J. E., Díaz-García, L. A., et al. 2022, *A&A*, 666, A84
- Graham, A. W., Janz, J., Penny, S. J., et al. 2017, *ApJ*, 840, 68
- Granato, G. L. & Danese, L. 1994, *MNRAS*, 268, 235
- Granato, G. L., De Zotti, G., Silva, L., Bressan, A., & Danese, L. 2004, *ApJ*, 600, 580
- Granato, G. L., Lacey, C. G., Silva, L., et al. 2000, *ApJ*, 542, 710
- Granato, G. L., Ragone-Figueroa, C., Taverna, A., et al. 2021, *MNRAS*, 503, 511
- Gu, Y., Fang, G., Yuan, Q., Cai, Z., & Wang, T. 2018, *ApJ*, 855, 10
- Guo, Q., White, S., Boylan-Kolchin, M., et al. 2011, *MNRAS*, 413, 101
- Harrold, J. E., Almaini, O., Pearce, F. R., & Yates, R. M. 2024, *MNRAS*, 532, L61
- Hasinger, G. 2008, *A&A*, 490, 905
- Henriques, B. M. B., Yates, R. M., Fu, J., et al. 2020, *MNRAS*, 491, 5795
- Hopkins, P. F., Quataert, E., & Murray, N. 2012, *MNRAS*, 421, 3522
- Krumholz, M. R., McKee, C. F., & Tumlinson, J. 2009, *ApJ*, 693, 216
- Lacerda, E. A. D., Sánchez, S. F., Cid Fernandes, R., et al. 2020, *MNRAS*, 492, 3073
- Lin, L., Hsieh, B.-C., Pan, H.-A., et al. 2019, *ApJ*, 872, 50
- Liske, J., Baldry, I. K., Driver, S. P., et al. 2015, *MNRAS*, 452, 2087
- Loveday, J., Norberg, P., Baldry, I. K., et al. 2012, *MNRAS*, 420, 1239
- Mahoro, A., Pović, M., Väisänen, P., Nkundabakura, P., & van der Heyden, K. 2022, *MNRAS*, 513, 4494
- Marasco, A., Fraternali, F., & Binney, J. J. 2012, *MNRAS*, 419, 1107
- Nandra, K., Georgakakis, A., Willmer, C. N. A., et al. 2007, *ApJ*, 660, L11
- Nelson, D., Pillepich, A., Springel, V., et al. 2018, *MNRAS*, 475, 624
- Nyiransengiyumva, B., Pović, M., Nkundabakura, P., & Mahoro, A. 2021, in *Nuclear Activity in Galaxies Across Cosmic Time*, ed. M. Pović, P. Marziani, J. Masegosa, H. Netzer, S. H. Negu, & S. B. Tessema, Vol. 356, 152–157
- Pandey, B. 2024, *MNRAS*, 530, 4550
- Parente, M., Ragone-Figueroa, C., Granato, G. L., et al. 2022, *MNRAS*, 515, 2053
- Parente, M., Ragone-Figueroa, C., Granato, G. L., & Lapi, A. 2023, *MNRAS*, 521, 6105
- Planck Collaboration, Ade, P. A. R., Aghanim, N., et al. 2014, *A&A*, 571, A16
- Rowlands, K., Wild, V., Bourne, N., et al. 2018, *MNRAS*, 473, 1168
- Salim, S. 2014, *Serbian Astronomical Journal*, 189, 1
- Sampaio, V. M., de Carvalho, R. R., Ferreras, I., Aragón-Salamanca, A., & Parker, L. C. 2022, *MNRAS*, 509, 567
- Schawinski, K., Urry, C. M., Simmons, B. D., et al. 2014, *MNRAS*, 440, 889
- Schawinski, K., Urry, C. M., Virani, S., et al. 2010, *ApJ*, 711, 284
- Silva, L., Granato, G. L., Bressan, A., & Danese, L. 1998, *ApJ*, 509, 103
- Silverman, J. D., Mainieri, V., Lehmer, B. D., et al. 2008, *ApJ*, 675, 1025
- Springel, V., White, S. D. M., Jenkins, A., et al. 2005, *Nature*, 435, 629
- Stringer, M. J., Bower, R. G., Cole, S., Frenk, C. S., & Theuns, T. 2012, *MNRAS*, 423, 1596
- Taylor, E. N., Hopkins, A. M., Baldry, I. K., et al. 2011, *MNRAS*, 418, 1587
- Trussler, J., Maiolino, R., Maraston, C., et al. 2020, *MNRAS*, 491, 5406
- Valiante, E., Smith, M. W. L., Eales, S., et al. 2016, *MNRAS*, 462, 3146
- Wang, T., Elbaz, D., Alexander, D. M., et al. 2017, *A&A*, 601, A63
- Wright, A. H., Robotham, A. S. G., Bourne, N., et al. 2016, *MNRAS*, 460, 765
- Wright, R. J., Lagos, C. d. P., Davies, L. J. M., et al. 2019, *MNRAS*, 487, 3740
- Wyder, T. K., Martin, D. C., Schiminovich, D., et al. 2007, *ApJS*, 173, 293